

Continuum models of the electrochemical diffuse layer in electronic-structure calculations

Francesco Nattino,¹ Matthew Truscott,² Nicola Marzari,¹ and Oliviero Andreussi²

¹*Theory and Simulations of Materials (THEOS) and National Centre for Computational Design and Discovery of Novel Materials (MARVEL), École Polytechnique Fédérale de Lausanne, CH-1015 Lausanne, Switzerland.*

²*Department of Physics, University of North Texas, Denton, TX 76207, USA.*

(Dated: 2 February 2022)

Continuum electrolyte models represent a practical tool to account for the presence of the diffuse layer at electrochemical interfaces. However, despite the increasing popularity of these in the field of materials science it remains unclear which features are necessary in order to accurately describe interface-related observables such as the differential capacitance (DC) of metal electrode surfaces. We present here a critical comparison of continuum diffuse-layer models that can be coupled to an atomistic first-principles description of the charged metal surface in order to account for the electrolyte screening at electrified interfaces. By comparing computed DC values for the prototypical Ag(100) surface in an aqueous solution to experimental data we validate the accuracy of the models considered. Results suggest that a size-modified Poisson-Boltzmann description of the electrolyte solution is sufficient to qualitatively reproduce the main experimental trends. Our findings also highlight the large effect that the dielectric cavity parameterization has on the computed DC values.

I. INTRODUCTION

The electrical double layer (DL) is of primary importance in the field of energy conversion, as it plays a crucial role in devices such as supercapacitors and fuel cells^{1,2}. The DL structure is essentially characterized by two layers of opposite charge that appear at the interface between an electrified surface and an electrolyte solution. This structure arises from the charge accumulation at the boundary of the solvated surface, which attracts counterions from the bulk solution. The balance between the electrostatic attraction towards the charged surface, the entropic electrolyte contributions, and the steric repulsion between the ions gives rise to an equilibrium charge distribution in the solution that is generally known as the diffuse layer.

Unfortunately, various limitations hamper atomistic simulations of the diffuse layer³. First, long simulation times are required in order to achieve statistically significant samplings of the solvent and electrolyte configurations, with the corresponding time-scales being often beyond the reach of standard first-principles molecular dynamics techniques. In addition, large simulation cells are necessary in order to capture the long-range screening of typical values of the surface charge densities.

Continuum models represent an attractive alternative to fully-atomistic models of electrolyte solutions. A continuum description of the solvent and of the ions allows, in fact, to bypass the computationally-intensive configurational sampling of the solution's degrees of freedom. In particular, our focus here is on hybrid methods, where a first-principles modeling of an electrified surface is coupled to a continuum description of the solution (Figure 1). These models are particularly appealing for the accuracy and predictive power that they can potentially have, as the processes occurring at or within the metal surface are described at a quantum-mechanical level, while the electrostatic screening of the diffuse layer is accounted for at a mean-field level.

Starting from highly simplified models of the double layer, which consist of a counter-charge plane at a fixed distance from a charged metal surface⁴⁻⁶, more complex diffuse layer models have been subsequently proposed and integrated into periodic density-functional theory (DFT) codes⁷⁻¹⁷. However, despite the large variety of electrolyte models proposed, there is no consensus on the model features required to achieve a physically-sound description of the diffuse layer. On one hand, full-continuum models that are based on the solution

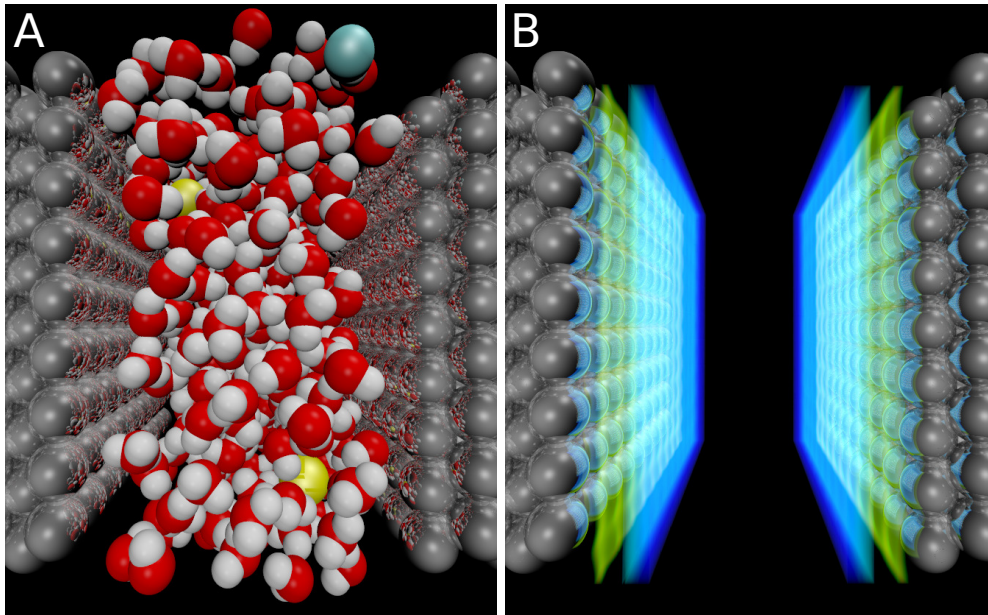


FIG. 1. Visualization of the atomistic details of a typical electrochemical setup (A): The metal slab (silver spheres) is in contact with an neutral aqueous solution (oxygen in red, hydrogen in white) containing electrolyte species (cyan and yellow spheres). Continuum models are obtained by integrating out the atomistic degrees of freedom of the mobile species (e.g. water and electrolytes) and replacing them with homogeneous continuum bodies, whose boundaries reflect the physical separation between the QM system and the environment. In B the solvent boundary (green transparent surface) is reported together with the continuous charge density of the electrolyte (blue transparent field), as computed for a charged substrate. Different onset for the solvent and electrolyte continuum models can be imposed in the definition of the model or can be obtained by including additional repulsive interactions between the continuum electrolyte and the QM substrate.

of some form of the size-modified Poisson-Boltzmann (PB) equation have been shown to qualitatively or semi-quantitatively describe experimental data^{18–20}. On the other hand, recent work from Sundararaman et al.¹⁶ has suggested that non-linear effects in the dielectric continuum also play an important role, and should thus be accounted for in order to reproduce measured trends.

In this work, we tackle these issues by systematically analyzing the performance of a hierarchy of continuum diffuse layer models of increasing complexity. We show how the various models can be derived from similar expressions of a free-energy functional and how they can be implemented in the framework of DFT. We choose the differential capacitance

(DC) of a model metal surface as a prototypical observable to compare and contrast the various electrolyte models. In particular, we consider a Ag(100) surface in an aqueous solution as study system, motivated by the availability of accurate experimental data²¹ that have been widely used in the literature to validate diffuse layer models^{15,16,18}.

Results show that a size-modified Poisson-Boltzmann model is able to qualitatively capture the main features of experimental DC curves, including the minimum capacitance value at the potential of zero charge, and the two local maxima at higher and lower potentials. The choice of solvation cavity employed to separate the quantum-mechanical region from the continuum solvent region is also found to play an important role on the absolute value of the computed DC.

The article is structured as follows. Section II reviews the theoretical background of the diffuse layer models considered and it presents the details of their computational implementations. Results on the computed DC values for the Ag(100) surface are then presented in Section III. In particular, the various electrolyte models are illustratively compared under vacuum conditions in Section III A, while their performance is better validated in Section III B by comparing results to experimental data. Finally, the conclusions are presented in Section IV.

II. METHODS

A. The Electrolyte Cavity

In the framework of continuum solvation models, the solvent's degrees of freedoms are smeared out in a continuum description and accounted for by means of a dielectric continuum. An important element in this class of models is represented by the so-called solvation cavity, which defines the boundary between the explicitly described solute region and the solvent region, where the dielectric continuum is located. This partitioning of the simulation cell can be formally defined through an interface function, $s(\mathbf{r})$. We define here $s(\mathbf{r}) \equiv 1$ inside the solute region, and $s(\mathbf{r}) \equiv 0$ in the region of space characterized by the solvent dielectric constant ϵ_0 . In the field of material science and condensed matter physics, continuum models typically involve interface functions that smoothly switch between the two regions, as they turn out to provide a considerable improvement to numerical stability^{22–24}. Closely

related to $s(\mathbf{r})$, the dielectric function $\varepsilon(\mathbf{r})$ sets the local value of the dielectric constant:

$$\varepsilon(\mathbf{r}) = 1 + (\varepsilon_0 - 1)(1 - s(\mathbf{r})). \quad (1)$$

In a similar fashion, the interface function $s(\mathbf{r})$ can be exploited to define the region of space that is accessible to the ionic species in the solution. In particular, the complementary interface function $\gamma(\mathbf{r})$ defines the portion of the cell where the electrolyte solution is located:

$$\gamma(\mathbf{r}) = 1 - s(\mathbf{r}). \quad (2)$$

It is important to stress here that in the above equations we have expressed both the solvent and the electrolyte domains in terms of the same interface function. In principle, since the two domains are associated with the regions of space that are accessible to solvent and electrolyte particles, respectively, different interface functions should be required. For example, electrolyte ions that have strong solvation shells may be hindered direct access to the electrochemical interface, their closest distance from the substrate being increased by the thickness of the coordinating solvent molecules in what is known as the Stern layer²⁵. In order to simplify the parameterization and tuning of the different interfaces, the electrolyte boundary is often expressed as a scaled version of the solvent one^{10,16,26,27}. Alternatively, a single interface is used and additional repulsive potentials are added to the free energy functional of the electrolyte system to stabilize solutions which are displaced from the solvent interface⁸. The latter approach has the additional flexibility of allowing both repulsive and attractive interactions between the components of the diffuse layer and the substrate. For this reason, we decided to focus the following discussion on models with a single common interface function.

The interface function $s(\mathbf{r})$ is typically constructed as a function of the solute's degrees of freedom. In order to explore how the choice of the solvation cavity affects the resulting diffuse layer model, we have considered the following three interface functions.

A first interface function is based on the local value of the solute's electron density. An optimally-smooth switching function has been proposed by Andreussi et al.²⁴, who have revised in the so-called self-consistent continuum solvation (SCCS) model the one originally proposed by Fattebert and Gigy²² and Scherlis et al.²³.

As a second interface function, we consider a rigid function of the solute's atomic positions, as defined through the product of atom-centered interlocking spheres with a smooth

erf-like profile. This cavity function, as proposed by Fisicaro et al. in the recent soft-sphere continuum solvation (SSCS) model²⁸, accounts for the diversity of the chemical species involved through tabulated van-der-Waals radii.

The last interface function reflects the two-dimensional character of the slab system considered. In particular, a planar boundary between solvent and solute is defined as a mere function of the vertical distance from the slab center, d . Two parameters are employed to define the cavity. The first one, d , defines the absolute position of the interface. The second one, Δ , regulates the smoothness of the boundary by defining the spread of the error-function profile which we have included along the surface normal. This simplified form of interface has not been explicitly addressed before in the literature. It has been introduced here to facilitate the comparison with analytical one-dimensional models. For particularly regular substrates it may provide an easier and more robust approach with respect to atomic-centered or electron-based interfaces.

B. The Electrolyte Models

In this section we describe the continuum electrolyte models considered and illustrate how they can be derived from specific free-energy functionals where we include all electrostatic and mean-field contributions (the usual non-interacting electron kinetic energy and the exchange-correlation energy terms are also included, but left out in the expressions for improved readability). In order to perform self-consistent DFT calculations for a system embedded in an electrolyte solution, energy contributions that explicitly depend on the solute electron density require the inclusion of corresponding terms in the Kohn-Sham (KS) potential. Furthermore, terms that explicitly depend on the solute’s atomic positions give rise to analogous contributions to the atomic forces. All these contributions are reported in the Supplemental Material.

In this work, we have neglected the solvent-related non-electrostatic contributions to the free-energy^{23,24} based on the quantum volume and quantum surface²⁹. Such contributions, however, can be straightforwardly included by adding corresponding terms to the free-energy, to the KS potential and to the forces^{23,24}.

1. Planar Countercharge Model

To first approximation, the electrolyte screening of the surface charge can be accounted for by introducing a countercharge plane at a given distance from the surface⁴. The presence of this external charge modifies the electrostatic energy of the system. When accounting for this electrostatic term, the free energy of the system embedded in the electrolyte solution can be computed as:

$$F^{PC}[\rho(\mathbf{r}), \phi(\mathbf{r})] = \int \left[-\frac{\varepsilon(\mathbf{r})}{8\pi} |\nabla \phi(\mathbf{r})|^2 + \rho(\mathbf{r}) \phi(\mathbf{r}) + \rho^{ions}(\mathbf{r}) \phi(\mathbf{r}) \right] d\mathbf{r} \quad (3)$$

Here $\rho(\mathbf{r})$ is the total (i.e. electronic + nuclear) charge density of the solute, $\phi(\mathbf{r})$ is the electrostatic potential and $\rho^{ions}(\mathbf{r})$ is the external charge density that mimics the counterion accumulation.

This model can be seen as a computational implementation of the Helmholtz model for the double layer³⁰: the countercharge plane completely screens the surface charge in a region of space that can be chosen to be infinitely narrow. Note that the Helmholtz screening does not depend on the ionic strength of the solution; it is thus not surprising that the bulk electrolyte concentration does not appear in Eq. 3.

2. Poisson-Boltzmann Model

A more physical description of the diffuse layer can be derived from a free-energy expression that accounts for the chemical potential and the entropy of the ions in the solution^{10,31}. These terms allow one to introduce an explicit dependence on the local concentrations of the electrolyte species ($\{c_i(\mathbf{r})\}$). For an electrolyte solution with p ionic species with charges $\{z_i\}$ and bulk concentrations $\{c_i^0\}$, such that the solution is overall neutral ($\sum_{i=1}^p z_i c_i^0 = 0$), the free energy functional takes the following form^{10,31}:

$$F[\rho(\mathbf{r}), \phi(\mathbf{r}), \{c_i(\mathbf{r})\}] = \int \left[-\frac{\varepsilon(\mathbf{r})}{8\pi} |\nabla \phi(\mathbf{r})|^2 + \rho(\mathbf{r}) \phi(\mathbf{r}) + \rho^{ions}(\mathbf{r}) \phi(\mathbf{r}) + \sum_{i=1}^p \mu_i (c_i(\mathbf{r}) - c_i^0) - T (s[\{c_i(\mathbf{r})\}] - s[\{c_i^0\}]) \right] d\mathbf{r}. \quad (4)$$

Here μ_i is the chemical potential of the i -th electrolyte species, T is the temperature, and $s[\{c_i\}]$ is the electrolyte entropy density per unit volume. The electrolyte charge density can be expressed in terms of the local electrolyte concentrations as $\rho^{ions}(\mathbf{r}) = \sum_{i=1}^p c_i(\mathbf{r}) z_i$.

Under the assumptions of a point-charge electrolyte and ideal mixing, the entropy density of the solution is:

$$s[\{c_i(\mathbf{r})\}] = -k_B \sum_{i=1}^p c_i(\mathbf{r}) \ln \frac{c_i(\mathbf{r})}{\gamma(\mathbf{r})}, \quad (5)$$

where k_B is the Boltzmann constant. Note that the exclusion function $\gamma(\mathbf{r})$, which sets the boundary between the electrolyte solution and the solute region, enforces a zero entropic contribution from the volume assigned to the quantum-mechanical region.

In order to find an expression for the equilibrium electrolyte concentrations, the free-energy functional in equation 4 is minimized with respect to $c_i(\mathbf{r})$. This procedure first leads to the condition:

$$z_i \phi(\mathbf{r}) - \mu_i + k_B T \left(\ln \frac{c_i(\mathbf{r})}{\gamma(\mathbf{r})} + 1 \right) = 0, \quad (6)$$

which allows one to obtain an expression for the chemical potential from the the bulk electrolyte region, where $\phi(\mathbf{r}) = 0$ and $\gamma(\mathbf{r}) = 1$, obtaining:

$$\mu_i = k_B T (\ln c_i^0 + 1). \quad (7)$$

By substituting equation 7 back into equation 6 one then obtains the following expression for the equilibrium electrolyte concentration:

$$c_i(\mathbf{r}) = \gamma(\mathbf{r}) c_i^0 e^{-\frac{z_i \phi(\mathbf{r})}{k_B T}} \equiv c_i^{PB}(\phi(\mathbf{r})) \quad (8)$$

By using this equilibrium electrolyte concentration, the free-energy functional expression significantly simplifies to:

$$F^{PB}[\rho(\mathbf{r}), \phi(\mathbf{r})] = \int \left[-\frac{\varepsilon(\mathbf{r})}{8\pi} |\nabla \phi(\mathbf{r})|^2 + \rho(\mathbf{r}) \phi(\mathbf{r}) + k_B T \sum_{i=1}^p c_i^0 \left(1 - \gamma(\mathbf{r}) e^{-\frac{z_i \phi(\mathbf{r})}{k_B T}} \right) \right] d\mathbf{r}. \quad (9)$$

Minimization of the free-energy functional with respect to $\phi(\mathbf{r})$ now leads to the well-known Poisson-Boltzmann equation (PBE), which allows one to relate the equilibrium charge densities in the system to the the electrostatic potential of the system:

$$\nabla \cdot \varepsilon(\mathbf{r}) \nabla \phi(\mathbf{r}) + 4\pi \sum_{i=1}^p z_i c_i^{PB}(\phi(\mathbf{r})) = -4\pi \rho(\mathbf{r}). \quad (10)$$

For low electrostatic potentials, i.e. whenever $z_i \phi(\mathbf{r}) \ll k_B T$, one can approximate the exponential dependence on $\phi(\mathbf{r})$ with a linear function:

$$e^{-\frac{z_i \phi(\mathbf{r})}{k_B T}} \approx 1 - \frac{z_i \phi(\mathbf{r})}{k_B T}. \quad (11)$$

The expression of the electrolyte concentrations thus reduces to:

$$c_i(\mathbf{r}) \approx \gamma(\mathbf{r}) c_i^0 \left(1 - \frac{z_i \phi(\mathbf{r})}{k_B T} \right) \equiv c^{LPB}(\phi(\mathbf{r})), \quad (12)$$

which leads to the following linearized-version of the PBE (LPBE):

$$\nabla \cdot \varepsilon(\mathbf{r}) \nabla \phi(\mathbf{r}) - k^2 \gamma(\mathbf{r}) \phi(\mathbf{r}) = -4\pi \rho(\mathbf{r}). \quad (13)$$

The constant operator $k^2 = 4\pi \frac{\sum_{i=1}^p z_i^2 c_i^0}{k_B T}$ is related to the Debye length λ_D of the electrolyte solution:

$$k^2 = \frac{\varepsilon_0}{\lambda_D^2}. \quad (14)$$

The LPBE can be equivalently derived²⁷ by Taylor-expanding the exponential term in Eq. 9 up to second order in $\phi(\mathbf{r})$, and by subsequently minimizing the resulting energy functional,

$$F^{LPB}[\rho(\mathbf{r}), \phi(\mathbf{r})] = \int \left[-\frac{\varepsilon(\mathbf{r})}{8\pi} |\nabla \phi(\mathbf{r})|^2 + \rho(\mathbf{r}) \phi(\mathbf{r}) + \right. \\ \left. - \frac{\sum_{i=1}^p z_i^2 c_i^0}{2k_B T} \gamma(\mathbf{r}) \phi^2(\mathbf{r}) + k_B T \sum_{i=1}^p c_i^0 (1 - \gamma(\mathbf{r})) \right] d\mathbf{r}, \quad (15)$$

with respect to the electrostatic potential.

The linear-regime of the PBE is expected to hold for a narrow potential range around the potential of zero charge (PZC). However, typical applications easily require the modeling of potential windows that extend for hundreds of mV, making it desirable to have efficient strategies to solve the full PB problem instead. If the interface between the solute and the electrolyte is suitable to a two-dimensional approximation, one can tackle the full PB problem by taking advantage of the reduced dimensionality of the interface. In particular, one can integrate out the dimensions in the surface plane and exploit the analytical solution of the PBE in one dimension⁹⁻¹¹. In the following, we assume for convenience that the system is oriented with the x axis perpendicular to the slab plane and that the diffuse layer starts at a distance x_{Stern} from the center of the slab. Taking the planar average of the physical quantities involved in Eq. 10 and assuming that the system charge density and the dielectric interfaces are fully contained within the x_{Stern} distance, the resulting one-dimensional differential equation

$$\frac{d^2 \phi(x)}{dx^2} = -\frac{4\pi}{\varepsilon_0} \left(\rho(x) + \sum_{i=1}^p z_i c_i(\phi(x)) \right) \quad (16)$$

can be integrated analytically for $|x| \geq x_{Stern}$. For the most common case of a diffuse layer composed by ions of equal concentrations c^0 and opposite signs, the electrostatic potential in the electrolyte region can be expressed as (see Supplemental material for the derivation):

$$\phi(x) = \frac{4k_B T}{|z|} \coth^{-1}(c_1 \exp(c_2 |x|)), \quad (17)$$

where $c_2 = 32\pi k_B T c^0 / \varepsilon_0$ and c_1 is obtained by imposing continuity of the normal component of the electric field at the electrolyte interface (i.e. for $x = x_{Stern}$). Only the solution with the correct asymptotic behavior has been selected, ensuring that $\phi(|x| \rightarrow \infty) = 0$. This model effectively corresponds to the Gouy-Chapman (GC) model for the diffuse layer^{32,33}, and shares the assumption of a planar distribution of charge at a fixed distance from the slab surface with the Helmholtz model described in Section II B 1. However, it includes a more physically sound shape of the diffuse layer along the surface normal. In the linearized regime, the one-dimensional solution of the electrostatic problem would instead be given by (see Supplemental material for the derivation):

$$\phi(x) = c_0 \exp\left(\frac{k}{\varepsilon_0} |x|\right) \quad (18)$$

where c_0 can be obtained by imposing continuity of the normal component of the electric field at the electrolyte interface.

For complex interfaces and general geometries, and for applications for which the linear-regime of the PBE is not expected to hold, one needs to numerically solve the full non-linear PBE (Eq. 10) to find the electrolyte concentration that minimizes the energy of the solvated system.

3. Size-Modified Poisson-Boltzmann Model

The standard PB model assumes point-like ions, and consistently overestimates the electrolyte countercharge accumulation at electrode surfaces. An improved model for the diffuse layer accounts for the steric repulsion between the ions, which opposes the electrostatic attraction towards the electrode surface and therefore limits electrolyte crowding. This is the so-called size-modified PB (MPB) model, which can be derived from the free-energy functional as in Eq. 4 but exploiting an entropy density expression that accounts for the finite-size of the ionic particles.

Borukhov et al.^{31,34} derived such an entropy expression from a lattice-gas model. In particular, the volume of the continuum solution is divided into a three dimensional lattice, with each cell of the lattice being occupied by no more than one ion. Thus, the cell volume a^3 or, equivalently, the maximum local ionic concentration $c_0 = \frac{1}{a^3}$, sets the distance of closest approach between ionic particles in the solution. In this framework, the solute region is not part of the continuum solution and should therefore give zero contribution to the solution entropy density. Otani and Sugino, who focused on two-dimensional slab systems, naturally achieved this limit by setting the boundary for the continuum solution region at a fixed distance from the surface⁷. In their derivations, Jinnouchi and Anderson⁸ have instead imposed such a limit through an effective repulsive interaction between solute and electrolyte, which prevents the electrolyte solution from entering the quantum-mechanical region. Ringe et al.^{27,35} have similarly accounted for such repulsive potential by recasting it in the form of an exclusion function. Here we follow a different approach^{9,10}, and enforce the limit by imposing a space-dependence for the maximum ionic concentration, consequently exploiting the complementary interface function $\gamma(\mathbf{r})$: $c_0 \equiv c_0(\mathbf{r}) = c_{max}\gamma(\mathbf{r})$. The final expression for the electrolyte entropy density is therefore:

$$s[\{c_i(\mathbf{r})\}] = -k_B \sum_{i=1}^p c_i(\mathbf{r}) \ln \frac{c_i(\mathbf{r})}{c_{max}\gamma(\mathbf{r})} + \\ - k_B \left(c_{max}\gamma(\mathbf{r}) - \sum_{i=1}^p c_i(\mathbf{r}) \right) \ln \left(1 - \sum_{i=1}^p \frac{c_i(\mathbf{r})}{c_{max}\gamma(\mathbf{r})} \right), \quad (19)$$

The first and second terms in Eq. 19 can be identified as the entropy contributions from the ions and the solvent, respectively. As in Eq. 5, the exclusion function $\gamma(\mathbf{r})$ sets the boundary of the region that contributes to the entropy of the electrolyte solution.

By minimizing the free-energy functional in Eq. 4 with respect to the ion concentration we obtain the following expressions for the electrolyte chemical potentials (cf. Eq. 7):

$$\mu_i = k_B T \ln \left(\frac{c_i^0}{c_{max} - \sum_{i=1}^p c_i^0} \right), \quad (20)$$

and for the equilibrium ionic concentrations (cf. Eq. 8):

$$c_i(\mathbf{r}) = \frac{\gamma(\mathbf{r}) c_i^0 e^{-\frac{z_i \phi(\mathbf{r})}{k_B T}}}{1 - \sum_{i=1}^p \frac{c_i^0}{c_{max}} \left(1 - e^{-\frac{z_i \phi(\mathbf{r})}{k_B T}} \right)} \equiv c_i^{MPB}(\phi(\mathbf{r})) \quad (21)$$

The denominator in Eq. 21 renormalizes the concentration in the regions where the electrostatic interaction energy is comparable to or larger than $k_B T$, and sets c_{max} as the maximum electrolyte concentration. This parameter can be related to the effective ionic radius r_i through $c_{max} = \frac{3P}{4\pi r_i^3}$. In the following, we will assume random close packing for the electrolyte particles and correspondingly set the packing efficiency $P = 0.64$. Note that the point charge limit of Eq. 21, which corresponds to $c_{max} \rightarrow \infty$, consistently leads to the equilibrium concentration as derived in the standard PB model (Eq. 8).

By substituting Eqs. 19-21 into Eq. 4, one obtains the following expression for the MPB free-energy functional:

$$F^{MPB}[\rho(\mathbf{r}), \phi(\mathbf{r})] = \int \left[-\frac{\epsilon(\mathbf{r})}{8\pi} |\nabla \phi(\mathbf{r})|^2 + \rho(\mathbf{r}) \phi(\mathbf{r}) + k_B T c_{max} \gamma(\mathbf{r}) \ln \left(c_{max} - \sum_{i=1}^p c_i^0 \right) + \right. \\ \left. - k_B T c_{max} \gamma(\mathbf{r}) \ln \left(c_{max} - \sum_{i=1}^p c_i^0 \left(1 - e^{-\frac{z_i \phi(\mathbf{r})}{k_B T}} \right) \right) \right] d\mathbf{r} - k_B T c_{max} V \ln \left(\frac{c_{max} - \sum_{i=1}^p c_i^0}{c_{max}} \right), \quad (22)$$

where V is the simulation cell volume. Minimization with respect to $\phi(\mathbf{r})$ finally leads to the size-modified Poisson-Boltzmann equation (MPBE), which is analogous to the standard PBE (Eq. 10) where, however, $c_i^{PB}(\phi(\mathbf{r}))$ is replaced by $c_i^{MPB}(\phi(\mathbf{r}))$.

4. Additional Interactions

The MPB model accounts for the steric repulsion between the ions in the solution, which limits electrolyte crowding. In addition, the solute and the ionic particles are expected to be surrounded by a solvation shell, where diffusing electrolyte particles are not expected to enter. The presence of this solvent-accessible but ion-free region, generally known as the Stern layer²⁵, can be simulated in a continuum framework via finite spacing between the onset of the dielectric function and the electrolyte charge density.

Such a spacing can be effectively introduced through an *ad-hoc* repulsive term between solute and electrolyte, $\varphi(\mathbf{r})$ ⁸. The repulsive interaction would therefore give rise to the following free-energy contribution:

$$E_{rep}[\{c_i(\mathbf{r})\}] = \sum_{i=1}^p \int c_i(\mathbf{r}) \varphi(\mathbf{r}) d\mathbf{r}, \quad (23)$$

and subsequently appear in the expression for the equilibrium electrolyte concentration:

$$c_i(\mathbf{r}) = \frac{\gamma(\mathbf{r}) c_i^0 e^{-\frac{z_i \phi(\mathbf{r}) + \varphi(\mathbf{r})}{k_B T}}}{1 - \sum_{i=1}^p \frac{c_i^0}{c_{max}} \left(1 - e^{-\frac{z_i \phi(\mathbf{r}) + \varphi(\mathbf{r})}{k_B T}} \right)} \quad (24)$$

As noted by Ringe et al.²⁷, a repulsive solute-electrolyte interaction can be recast in the form of an electrolyte-specific exclusion function $\alpha(\mathbf{r}) \equiv e^{-\frac{\varphi(\mathbf{r})}{k_b T}}$. The exclusion function alone prevents the electrolyte from approaching and entering the solute region in their Stern-corrected MPB model. The exclusion function $\gamma(\mathbf{r})$ that appears in our model has a different physical origin, since it reflects the hard separation between quantum-mechanical and continuum regions. While the presence of the Stern layer could be effectively included in our model by using separate interface functions for dielectric and electrolyte, as for instance done by Dabo et al.^{9,10}, we find the picture of a single interface setting the boundary between quantum solute and continuum solution more physically sound. We thus resort to repulsive interactions to introduce the finite spacing between the onsets of the dielectric and the electrolyte fluids. Note that, similarly to Ringe's model, our approach also predicts a zero entropic contribution from the Stern-layer volume (cf. Eq. 19), which is consistent with the expected absence of diffusing solvent and electrolyte particles in this region.

For a two-dimensional system like a metal slab, we find appropriate to use one-dimensional exponential functions to define the repulsion potential:

$$\varphi(x) = e^{-\frac{|x-x_0|-d}{w}}, \quad (25)$$

where x_0 corresponds the x coordinate of the slab center and the parameters d and w set the position and decay rate of the potential, respectively.

Baskin and Prendergast²⁰ have proposed a similar formalism to account for the specific adsorption of electrolyte species. In particular, they have used a Morse-like potential in a fully-continuum model to mimic anion adsorption on the electrode surface:

$$\varphi(x) = E_{ads} \left(\left(1 - e^{-\frac{|x-x_0|-d}{w}} \right)^2 - 1 \right), \quad (26)$$

where E_{ads} is the anion adsorption energy and d now defines the distance between the surface plane and the adsorbed anion species. We have tested the introduction of such an interaction term in our mixed first-principles-continuum model. This description is computationally attractive as it bypasses the need for surface configuration and adsorbate coverage samplings.

However, it is clear that such a model cannot be expected to capture electronic-structure changes of the metal surface beyond mean-field electrostatic effects.

C. Computational Implementations

1. *Planar Countercharge Model*

For all the models presented here, calculations are performed in a symmetric setup: the electrode surface is modeled by means of a two-dimensional slab exposing two identical faces to the continuum solution. The computational setup thus involves two metal-solvent interfaces. Two charge distributions are added in front of the outermost atomic layers to compensate for the net charge of the surface, q .

For numerical reasons, the sharp countercharge plane that characterizes the Helmholtz model for the diffuse layer is broadened to have a Gaussian-shaped profile along the surface normal direction x :

$$\rho_{ions}^{Helmholtz}(x) = \frac{q}{2A\sqrt{\pi}\Delta} e^{-\frac{(|x-x_0|-d)^2}{\Delta^2}}, \quad (27)$$

where A is the surface area and the factor 2 at the denominator of the prefactor arises from the symmetric setup employed. The distance d from the slab center x_0 and the spread parameter Δ constitute the only two parameters in the model.

The countercharge distributions are straightforwardly added to the total charge of the system. The corresponding electrostatic potential does not require self-consistency, allowing for fast and stable simulations.

2. *Analytic Planar-Averaged Poisson-Boltzmann Model*

In many ways, modeling the diffuse layer via the analytical one-dimensional solution to the Poisson-Boltzmann problem can be seen as a straightforward modification of the Helmholtz approach, in which the shape of the planar countercharges is no longer given by a Gaussian envelope of arbitrary spread, but rather obtained from a physically sound model. However, simply inserting the diffuse layer as a charge distribution in the simulation cell would incur significant numerical problems: the analytical results for the electrolyte concentrations can present very sharp features close to the interface, which cannot be described accurately

with the standard numerical resolution of the electronic-structure calculation. Additionally, diffuse layers may have very long decaying length-scales, extending for tens of nanometers from the electrochemical interface, thus requiring large simulation cells. For these reasons, when possible a description in terms of the effects of the diffuse layer on the quantum-mechanical system, i.e. its electrostatic potential, is preferred.

The assumption behind the model is the one of two sharp interfaces at a fixed distance x_{Stern} from the slab center x_0 , above and below the slab: the quantum-mechanical system is fully contained within the two interfaces, while the diffuse layer is fully in the outer regions and is uniform along the yz planes perpendicular to the slab normal. With this setup, the net effect of the diffuse layer on the system would be a uniform shift, $\Delta\phi^{DL}$, of the electrostatic potential in the quantum-mechanical region of space, provided that the latter is computed with open-boundary conditions (OBC) along the x axis. Thus, a possible definition of the full potential in the simulation cell is represented by

$$\phi(\mathbf{r}) = \begin{cases} \phi^{OBC}(\mathbf{r}) + \Delta\phi_0^{DL} & |x - x_0| < x_{Stern} \\ \phi^{DL}(x) & |x - x_0| \geq x_{Stern} \end{cases}, \quad (28)$$

where ϕ^{DL} is given by Eqs. (17) or (18), and the shift is computed as

$$\Delta\phi_0^{DL} = \phi^{DL}(x_{Stern}) - \langle \phi^{OBC} \rangle_{yz}(x_{Stern}). \quad (29)$$

Since the quantum-mechanical system is not bound to be perfectly homogeneous in the yz plane, its planar average, $\langle \phi^{OBC} \rangle_{yz}(x) = A^{-1} \int \int \phi^{OBC}(\mathbf{r}) dy dz$, is used in the above equation, where A is the surface area in the simulation cell. As a consequence, discontinuities can be present in the potential of Eq. (28) when passing through the x_{Stern} interfaces. Even though these discontinuities happen in a region of space which is not occupied by the quantum-mechanical system, they may be a source of numerical instabilities. To overcome this limitation, a slightly different path can be followed, where the diffuse-layer contribution to the potential is expressed as a one-dimensional continuous and smooth correction defined in the whole simulation cell, namely

$$\phi(\mathbf{r}) = \phi^{OBC}(\mathbf{r}) + \Delta\phi^{DL}(x) \quad (30)$$

where

$$\Delta\phi^{DL}(x) = \begin{cases} \Delta\phi_0^{DL} & |x - x_0| < x_{Stern} \\ \phi^{DL}(x) - \langle \phi^{OBC} \rangle_{yz}(x) & |x - x_0| \geq x_{Stern} \end{cases}. \quad (31)$$

The planar average of the potential on the right-hand side of the above equation can then be approximated by the one-dimensional potential of a planar-averaged charge distribution, namely

$$\langle \phi^{OBC} \rangle_{yz} (|x - x_0| > x_{Stern}) \approx \langle \phi^{OBC} \rangle_{yz} (x_{Stern}) - \frac{2\pi q}{A\epsilon_0} |x - x_{Stern}|, \quad (32)$$

where q is the total charge of the quantum-mechanical system and we have used the classical electrostatics result for the potential of a planar charge distribution. With the above formulation, the correction and its first derivative are both continuous at the interface.

While the correction described here is similar in spirit to the ‘electrochemical boundary conditions’ from Refs.^{9–11}, our approach makes use of the electrostatic potential that analytically solves the PBE in order to determine the diffuse-layer contribution to $\phi(\mathbf{r})$, without the need of an iterative procedure. Another novel element of the procedure described is the implementation of the correction that corresponds to the linear-regime version of the PB problem, which allows for the validation of the corresponding numerical approach.

While the above correction is defined for open-boundary conditions, standard electronic-structure simulations usually exploit periodic-boundary conditions. In this case, an alternative expression of the electrostatic potential of the electrochemical interface can be obtained, which incorporates the handling of PBC artifacts and of the diffuse layer into a single continuous and smooth one-dimensional correction. In particular, an approximate OBC potential is obtained as

$$\phi^{OBC}(\mathbf{r}) \approx \phi^{PBC}(\mathbf{r}) + \Delta\phi^{2D}(x) \quad (33)$$

and assuming a planar-averaged charge distribution a parabolic correction can be expressed as³⁶

$$\Delta\phi^{2D}(x) = \frac{\alpha_{1D}}{L_x} q - \frac{2\pi q}{V} x^2 + \frac{4\pi}{V} d_x x - \frac{2\pi}{V} Q_{xx}, \quad (34)$$

where $\alpha_{1D} = \pi/3$ is the Madelung constant of a one-dimensional lattice, V is the cell volume, q , d_x , and Q_{xx} are the monopole, dipole, and quadrupole moments along the x axis of the charge distribution. The corrected electrostatic potential can thus be easily expressed in terms of the PBC one as

$$\phi(\mathbf{r}) \approx \phi^{PBC}(\mathbf{r}) + \Delta\phi^{2D}(x) + \Delta\phi^{DL}(x). \quad (35)$$

The above approach can be adopted for any situation where an analytical one-dimensional solution to the electrostatic problem is available. In the description of the diffuse layer, both

the Gouy-Chapman model and its linearized version have analytical solutions that can be inserted into the $\phi^{DL}(x)$ term. Although based on a planar-average approximation, this class of correction approaches has significant advantages, in terms of speed and stability, when compared to more advanced numerical solutions of the electrostatic equations.

3. *Linearized Poisson-Boltzmann Model*

In order to tackle the linear-regime version of the PB problem, we solve the corresponding differential equation using a preconditioned gradient-based method as proposed by Fiscaro et al.³⁷, which we will only summarize here. Briefly, we apply a conjugate-gradient algorithm to solve the LPBE:

$$\underbrace{(\nabla \cdot \varepsilon(\mathbf{r}) \nabla - k^2 \gamma(\mathbf{r}))}_{\mathbf{A}} \phi(\mathbf{r}) = \underbrace{-4\pi\rho(\mathbf{r})}_{b(\mathbf{r})}, \quad (36)$$

using the following preconditioning operator:

$$\mathbf{P} = \sqrt{\varepsilon(\mathbf{r})} \nabla^2 \sqrt{\varepsilon(\mathbf{r})} \quad (37)$$

Therefore, instead of minimizing the residual function $r(\mathbf{r}) = b(\mathbf{r}) - \mathbf{A}\phi(\mathbf{r})$, one finds the solution of the problem by minimizing the preconditioned residual $v(\mathbf{r}) = \mathbf{P}^{-1}r(\mathbf{r}) = \mathbf{P}^{-1}(b(\mathbf{r}) - \mathbf{A}\phi(\mathbf{r}))$. The algorithm has been proven to converge in a limited number of iterations for simple analytical cases³⁷. In addition, the choice of the preconditioner minimizes the computational effort required³⁷. In fact, the action of the operator \mathbf{A} on the preconditioned residual $v_n(\mathbf{r})$, which needs to be computed at each of the n -th solver's iteration, can be efficiently estimated as:

$$\begin{aligned} \mathbf{A}v_n(\mathbf{r}) &= (\nabla \cdot \varepsilon(\mathbf{r}) \nabla - k^2 \gamma(\mathbf{r})) v_n(\mathbf{r}) \\ &= (\varepsilon(\mathbf{r}) \nabla^2 + \nabla \varepsilon(\mathbf{r}) \cdot \nabla - k^2 \gamma(\mathbf{r})) v_n(\mathbf{r}) \\ &= -(q(\mathbf{r}) + k^2 \gamma(\mathbf{r})) v_n(\mathbf{r}) + r_n(\mathbf{r}), \end{aligned} \quad (38)$$

where $q(\mathbf{r}) = \sqrt{\varepsilon(\mathbf{r})} \nabla^2 \sqrt{\varepsilon(\mathbf{r})}$ and we have used $r_n(\mathbf{r}) = \mathbf{P}v_n(\mathbf{r}) = \varepsilon(\mathbf{r}) \nabla^2 v_n(\mathbf{r}) + \nabla \varepsilon(\mathbf{r}) \cdot \nabla v_n(\mathbf{r}) + q(\mathbf{r}) v_n(\mathbf{r})$. The term $q(\mathbf{r})$ can be evaluated only once and stored in memory. Once the terms $r_n(\mathbf{r})$ and $v_n(\mathbf{r})$ are computed, the evaluation of $\mathbf{A}v_n(\mathbf{r})$ at each of the following iterations requires only vector-vector multiplications. The bottleneck of the algorithm is

represented by the calculation of $v_n(\mathbf{r})$, which is calculated as³⁷:

$$v_n(\mathbf{r}) = \mathbf{P}^{-1} r_n(\mathbf{r}) = \frac{1}{\sqrt{\varepsilon(\mathbf{r})}} (\nabla^2)^{-1} \left(\frac{r_n(\mathbf{r})}{\sqrt{\varepsilon(\mathbf{r})}} \right). \quad (39)$$

The overall algorithm performance is thus highly dependent on the solution of the standard Poisson problem, which in our case is carried out in reciprocal space. The term $r_n(\mathbf{r})$ is computed instead from the knowledge of the residual function at the previous step $r_{n-1}(\mathbf{r})$ and other quantities derived from the preconditioned residual $v_n(\mathbf{r})$ ³⁷, as typically carried out in conjugate-gradient approaches.

While the algorithm from Fiscaro *et al.* was tested in Ref.³⁷ by solving the LPBE only for simple analytic potentials, we investigate here for the first time the performance of such preconditioned conjugate-gradient algorithm for realistic electrified interfaces through our novel implementation in the ENVIRON module³⁸ for Quantum ESPRESSO^{39,40}.

4. *Standard and Size-Modified Poisson-Boltzmann Model*

The preconditioned conjugate gradient algorithm from Ref.³⁷ can only tackle linear problems, like the one represented by the linearized-PB equation. Fiscaro *et al.* have also proposed an iterative algorithm devised to solve the full non-linear PB equation³⁷, which, however, turned out not to be sufficiently stable to deal with extended charged systems. For the numerical solution of the full (size-modified) PB equation, we thus resort to the more robust Newton-based algorithm as proposed by Ringe *et al.*²⁷, which we have also implemented in the development version of the ENVIRON module³⁸. In particular, the free-energy functional minimization that leads to the PB equation is recast as a root-finding problem:

$$G[\phi(\mathbf{r})] = 0, \quad (40)$$

where $G[\phi_n(\mathbf{r})]$ is the $\phi(\mathbf{r})$ functional derivative of the free-energy $F[\phi(\mathbf{r})]$:

$$G[\phi_n(\mathbf{r})] = \nabla \cdot \varepsilon(\mathbf{r}) \nabla \phi_n(\mathbf{r}) + 4\pi\rho(\mathbf{r}) + 4\pi \sum_i^p z_i c_i(\phi_n(\mathbf{r})), \quad (41)$$

Following Newton's iterative algorithm, the estimate for $\phi(\mathbf{r})$ at the the n -th step is obtained as:

$$\phi_{n+1}(\mathbf{r}) = \phi_n(\mathbf{r}) + \frac{G[\phi_n(\mathbf{r})]}{G'[\phi_n(\mathbf{r})]}. \quad (42)$$

Here $G'[\phi_n(\mathbf{r})]$ is the Fréchet derivative of $G[\phi_n(\mathbf{r})]$:

$$G'[\phi_n(\mathbf{r})] = \nabla \cdot \varepsilon(\mathbf{r}) \nabla + 4\pi \sum_i^p z_i \frac{\partial c_i}{\partial \phi}(\phi_n(\mathbf{r})). \quad (43)$$

By rearranging the terms in Eq. 42, the following linear problem is recovered:

$$\left(\nabla \cdot \varepsilon(\mathbf{r}) \nabla + 4\pi \sum_i^p z_i \frac{\partial c_i}{\partial \phi}(\phi_n(\mathbf{r})) \right) \phi_{n+1}(\mathbf{r}) = -4\pi \left(\rho(\mathbf{r}) + \sum_i^p z_i c_i(\phi_n(\mathbf{r})) - \sum_i^p z_i \frac{\partial c_i}{\partial \phi}(\phi_n(\mathbf{r})) \phi_n(\mathbf{r}) \right). \quad (44)$$

Overall, the algorithm proceeds as follows: starting from an initial guess for $\phi(\mathbf{r})$, i.e. $\phi_0(\mathbf{r})$, the charge and screening terms in Eq. 44 are evaluated. The new guess for the electrostatic potential, $\phi_1(\mathbf{r})$, is then determined by solving the corresponding linear problem using the preconditioned conjugate-gradient procedure from Ref.³⁷, as described in Section II C 3. The charge and screening terms are updated, and the new linear problem solved to find $\phi_2(\mathbf{r})$. These steps are repeated until convergence is achieved.

D. Computational Details

All the electrolyte models discussed have been implemented in the developer version of the ENVIRON module³⁸ for the Quantum ESPRESSO distribution^{39,40}. Differential capacitances have been calculated by numerically differentiating charge-potential curves. We have employed a canonical approach: we perform constant charge calculations and determine the applied potential U *a posteriori* from the difference between the asymptotic electrostatic potential and the Fermi energy of the system. Experimental data and simulations have been compared to each other using as potential reference the corresponding estimate of the potential of zero charge. In the simulations, this is the potential computed for a neutrally-charged surface, U_{PZC} (see Figure 2).

All calculations have been performed using the Perdew-Burke-Ernzerhof exchange-correlation functional^{41,42} and pseudo-potentials from the GBRV set⁴³, which have been chosen according to guidelines from the Standard Solid-State Pseudopotential library⁴⁴ (SSSP efficiency 0.7). Cutoff energies for the plane wave and density expansions have been set to 35 Ry and 350 Ry, respectively. A Γ -centered 18x18x1 k-point grid (or equivalent)

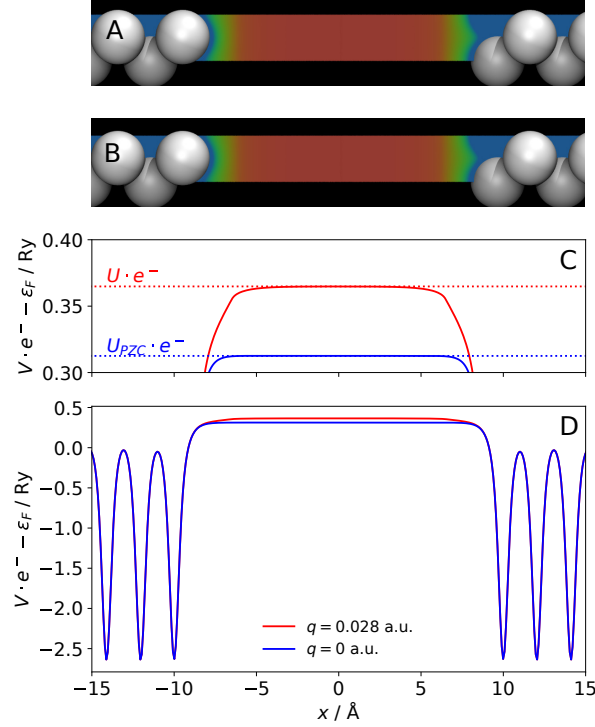


FIG. 2. 2D-maps of the electrostatic potential computed with the planar-averaged analytical PB model (A) and the corresponding numerical version (B) for a Ag(100) slab in vacuum with a total charge $q = 0.028$ a.u.. The planar-averaged electrostatic potential computed for the neutral and the charged surface (red and blue, respectively) is plotted as a function of the surface normal direction x in C and D. The same data is plotted in the C and D panels, using different scales for the potential axis. The planar interface with a symmetric monovalent electrolyte with bulk concentration $c_0 = 0.1$ M has been employed.

has been employed to sample the first Brillouin zone, using the cold smearing technique from Ref.⁴⁵ with smearing parameter $\sigma = 0.01$ Ry.

The Ag(100) slab has been constructed using 8 atomic layers at the bulk equilibrium lattice constant (4.149 \AA). The slab has been fully relaxed only in vacuum. While electrolyte- and solvent-related contributions to the atomic forces are accounted for and they in principle allow for fully self-consistent optimizations in the presence of the embedding continuum, test calculations for the present case show that further relaxations in implicit solvent negligibly affect the surface structure and the Fermi energy of the system.

Particular care needs to be taken with respect to the simulation cell size when using

the SSCS (‘soft-sphere’) cavity. If the diameter of the atom-centered spheres exceeds one of the cell lattice vectors, a sharp transition arises in the region where the spheres overlap with their neighboring periodic replicas, which can trigger numerical instabilities. In order to obtain a smooth interface function, one has to set the simulation cell size such that all the sphere diameters fit the simulation box. For this reason, calculations using the SSCS have been performed in a (2x2) supercell. We also note that the Ag sphere radii as part of the original SSCS parameterization²⁸ are such that the resulting cavity includes non-physical dielectric pockets inside the metal slab. This issue has been fixed by introducing a non-local correction based on the convolution of the interface function with a solvent-size-related probe function. In this way, dielectric pockets that are smaller than the chosen solvent molecule (in this case water) can be identified and removed. Further details on the construction of such non-local interface are deferred to a forthcoming publication⁴⁶.

The models characterized by a self-consistent optimization of the ionic countercharge density require large separations between periodic replicas of the slab along the surface normal. This is to account for the long-range electrolyte screening, whose typical length is the Debye length λ_D . Due to the partial screening of the electrolyte charge by the dielectric, calculations that include implicit solvent require larger cell sizes along the surface normal. We have verified that Fermi energies are converged within few meVs for a 20 Å (60 Å) separation between periodic images for calculations in vacuum (implicit solvent). For calculations involving particularly low bulk ionic concentrations (≤ 0.04 M) we have doubled these spacings. Note that the planar-averaged implementation of the PB model does not require these large spacings, as one resorts to the analytical solution of the one-dimensional problem to set the electrostatic potential at the cell boundaries. Such calculations have been thus performed with a spacing of 20 Å between periodic images. For both the numerical and analytic electrolyte models, we have made use of the parabolic corrective scheme from Ref.³⁶ in order to recover the potential of the isolated system from the electrostatic potential computed with periodic-boundary conditions (see also Equations 33 and 34). This correction guarantees that the electrostatic potential approaches zero at large distances from the metal slab, provided that enough empty space is included in the unit cell for the numerical models. While charge neutrality is often enforced by means of a Lagrange multiplier μ_{el} in the search for the electrostatic potential $\phi(\mathbf{r})$ that minimizes the energy of the system^{13,17,47}, the asymptotically-zero reference potential can be used with $\mu_{el} \equiv 0$. This choice simultaneously

provides the correct asymptotic limits for the electrolyte charge density and for the ionic concentration profiles¹⁷.

III. RESULTS AND DISCUSSION

A. Vacuum

We start by considering the differential capacitance (DC) of Ag(100) in a solution with the vacuum dielectric constant ($\epsilon_0 = 1$), which allows us to disentangle the electrolyte effects from the role played by the dielectric medium.

We first consider the planar-countercharge Helmholtz model (see Sections II B 1 and II C 1), which represents the lowest-rung diffuse layer model among the ones considered here. Figure 3 illustrates how the two parameters in the model, i.e. the surface-countercharge distance d and the spread of the charge distribution Δ , affect the computed DC. Overall, charge-potential curves are found to be close to linear for all tested parameter values. The DC predicted by the Helmholtz model is thus almost potential independent, with a small DC decrease for increasing potentials. This trend is consistent with the larger electron-density spilling at more negative potentials, which effectively reduces the distance between the surface and the fixed countercharge distribution. This simple capacitor model also explains the effect of the d parameter on the computed DC, as we observe an increase (decrease) of the DC value for an inward (outward) shift of the neutralizing counterion density. The broadening of the electrolyte charge density, as regulated by the Δ parameter, instead has a negligible effect on the DC. This is expected, as the spread of the distribution only affects the field in the narrow region where the countercharge is located. In contrast, the electrostatic potential at large distances from the countercharge planes is essentially unaffected by the Δ parameter, and so is the DC.

As already mentioned in Section II B 1, the Helmholtz model for the diffuse layer does not include any dependence on the bulk electrolyte concentration. The planar-averaged PB model overcomes this limitation while retaining the assumption of a planar countercharge-density profile. Results obtained with the linearized-PB model (see Sections II B 2 and II C 2) are illustrated in Figure 4, which shows the computed charge-potential curves and corresponding capacitance values for three representative electrolyte concentrations. The

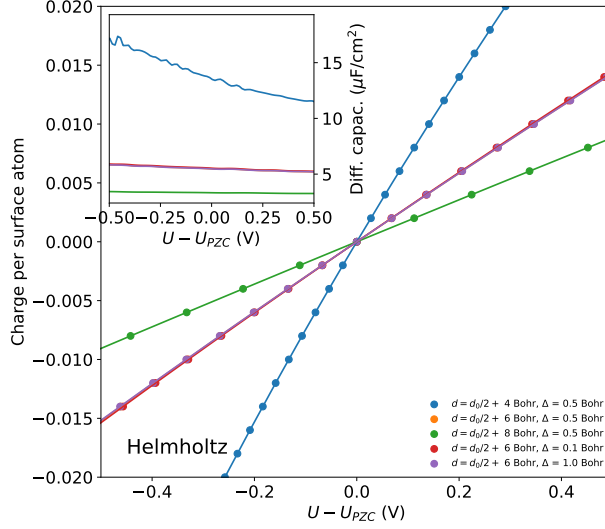


FIG. 3. The charge per surface atom (in a.u.) is plotted as a function of the potential (in V). The Helmholtz model has been used for all data sets, varying the d and Δ parameters that define the position and the width of the countercharge density, respectively. Note that the three lines corresponding to $d = d_0/2 + 6 \text{ Bohr}$ are essentially superimposed (d_0 is the slab thickness). The inset shows the differential capacitance as a function of the potential, as calculated from the analytical derivative of the spline-interpolated charge-potential curves (same line styles as in the main plot).

linear-regime PB model predicts a weak potential dependence of the DC, as also observed for the Helmholtz model, but the computed capacitance now depends on the electrolyte concentration. In particular, lower DC values correspond to lower ionic concentrations.

Figure 4 also includes results of calculations performed with the numerical linearized PB solver (see Sections II B 2 and II C 3), using a planar but smooth interface function with an error-function profile along the surface normal. We have used here a small spread parameter (0.01 Bohr) in order to better compare results to the planar-averaged LPB model, in which a sharp planar interface defines the boundary of the region where the one-dimensional LPBE is analytically solved. The DC computed through the numerical solution of the LPBE agrees well with what obtained through the corresponding planar-averaged analytic model. This is consistent with the interface being essentially two-dimensional, as expected for closely-packed metal surfaces like Ag(100).

The capacitance-potential trends obtained from the solution of the full-PBE (see Sec-

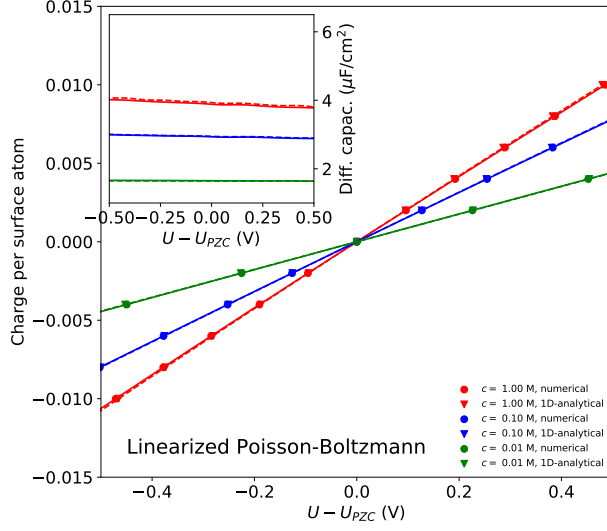


FIG. 4. Same as Figure 3, but for the planar-averaged analytic linearized-PB model (triangles and dashed lines) and the corresponding numerical implementation (circles and solid lines). Red, blue and green symbols correspond to bulk electrolyte concentrations $c_0 = 1$ M, $c_0 = 0.1$ M and $c_0 = 0.01$ M, respectively. x_{Stern} in the analytic model (Section II C 2) and d in the planar interface employed in the numerical model (Section II C 3) are set so that the interface lies in both cases 6.568 Bohr away from the surface.

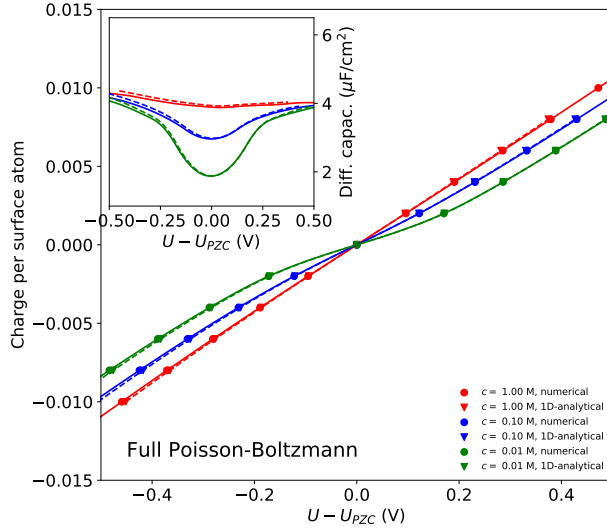


FIG. 5. Same as Figure 4, but for the full PB model, in the planar-averaged analytic implementation (triangles and dashed lines) and the numerical implementation (circles and solid lines).

tions IIB 2 and IIC 4) are quite different, as illustrated in Figure 5. In contrast with the linear-regime model, the DC curves computed with the non-linear electrolyte model exhibit a concentration-dependent drop at the potential of zero charge (PZC), while similar capacitance values are observed at the largest potentials simulated for all electrolyte concentrations (see also Figs. 4-10 and 4-11 of Ref.⁹). As also observed for the linearized model, we find very good agreement between the capacitance curves computed with the planar-averaged approach, which exploits the analytical solution of the PBE along the surface normal, and the full numerical implementation. As illustrated in Figure 2, in fact, the electrostatic potential obtained with the numerical model is not significantly corrugated in the yz -plane at sufficiently large distance from the surface, and is thus very similar to the potential computed with the planar-averaged analytical approach.

The effect of the interface broadening on the DC is illustrated in Figure 6, where we compare DC-potential curves computed with the numerical solver of the full-PBE (Section IIC 4) and a planar but smooth interface function. We have tested different values of the spread parameter Δ , ranging from 0.01 to 0.5 Bohr. The DC is found to increase for increasing values of Δ , which follows from the onset of the electrolyte-accessible region becoming closer to the surface. This effect is most pronounced at large (absolute) potentials and at high electrolyte concentrations. Under such conditions, in fact, the electrolyte charge density at the interface boundary is larger and sharper, and thus more sensitive to small changes in the onset region.

Figure 7 compares charge-potential curves and the corresponding DC values as computed with the numerical PB solver (Section IIC 4) paired to the three different cavities presented in Section IIA. Specifically, we have tested the use of the planar interface function also used in Figure 5 and 6 (see Figure 7A), and two additional cavities derived from the SSCS²⁸ (Figure 7B) and from the SCCS²⁴ (Figure 7C) models, respectively. To better compare results across the cavities employed, we choose the corresponding parameters so that the onsets of the three interface functions lie at approximately the same distance from the metal surface under neutral conditions, and a similar broadening characterizes the three interfaces.

Very similar DC-potential curves are obtained using the planar and SSCS cavities. The former produces slightly higher capacitance values, consistently with the electrolyte charge density more closely approaching interstitial surface regions with the soft-sphere interface. Both interfaces predict DC-potential curves that are asymmetric around the PZC, with

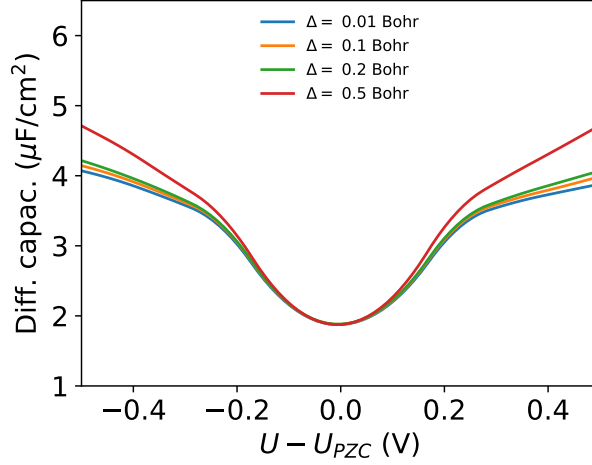


FIG. 6. Full Poisson-Boltzmann model: differential capacitance as a function of the potential for various values of the spread parameter Δ in the planar interface function, using the numerical solver. The distance parameter d has been set so that the interface lies 6.568 Bohr away from the surface. The full numerical PB model has been used for all calculations, using $c_0 = 0.01$ M.

slightly larger DC values at negative potentials as compared to the corresponding positive values. This is again consistent with the effective separation between the surface and the ionic density onset becoming smaller at negative potentials due to the larger electron density spilling towards the rigid electrolyte interface. Interestingly enough, the trend observed with the SCCS cavity is reversed. This density-dependent interface function, in fact, shifts the ionic density onset further away from the surface as the slab charge becomes more negative, effectively increasing the electrolyte-slab separation.

Figure 7 also includes results from the linearized PB model for the three cavities considered. This model correctly predicts the DC values at the PZC and the qualitative DC dependence on the bulk electrolyte concentration. Note that the capacitance computed with this model approaches the infinite-screening limit represented by the Helmholtz model capacitance for increasing ionic concentrations (Figure 7A). As also evident from comparing Figure 4 to Figure 5, the linearized version of the PB model dramatically fails in reproducing the potential trend computed with the corresponding non-linear model and it returns weak potential dependences with no minimum at the PZC. The monotonic trends observed for the linear-regime model are consistent with the patterns described for the corresponding non-linear model. For instance, the density-dependent SCCS cavity predicts monotonically

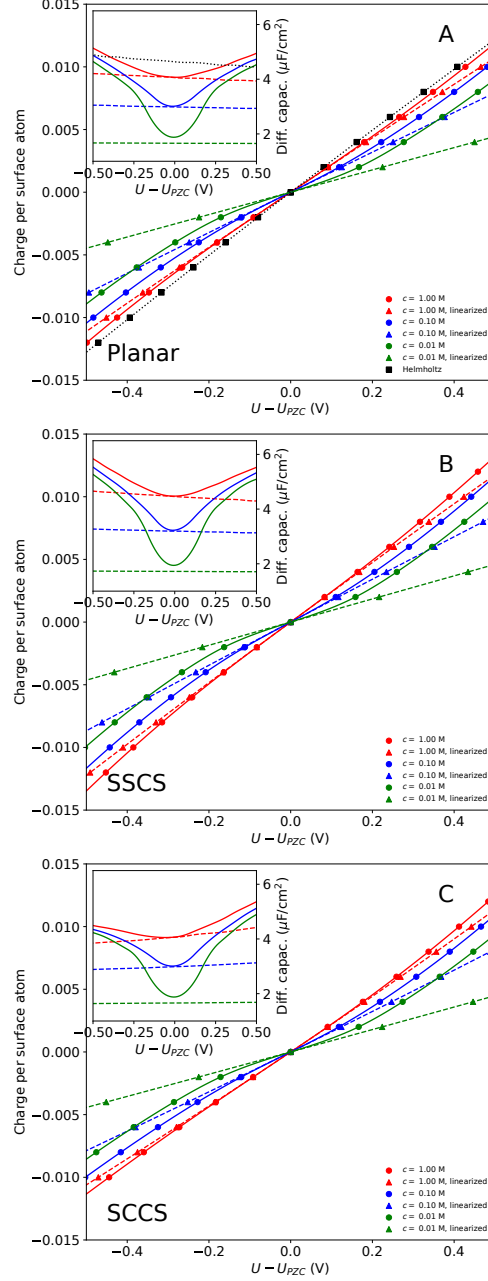


FIG. 7. Same as Figure 5, but for the full-numerical PB model (circle and solid lines) and linearized PB model (triangles and dashed lines). The interface functions employed are the following: the planar interface (top, $d = d_0/2 + 6.568$ Bohr, where d_0 is the slab thickness, and $\Delta = 0.470$ Bohr); the soft-sphere interface (middle, $r = 6.568$ Bohr, $\Delta = 0.470$ Bohr); and the SCCS interface (bottom, $\rho_{max} = 10^{-4}$ a.u. and $\rho_{min} = 10^{-5}$ a.u.). The top subplot also includes results obtained with the Helmholtz model (black squares and dotted line) as a comparison. The same d and Δ parameters used for the planar interface have been employed to set the Gaussian countercharge density.

increasing capacitance curves, as the surface-electrolyte gap increases with increasing potential. This is also consistent with the findings of Letchworth-Weaver and Arias¹², who have similarly observed monotonically increasing capacitance curves using a linearized-PB model for the diffuse layer and a density-dependent interface function.

Figure 8 compares DC curves computed using the standard (non-linear) PB model to results from the size-modified PB model (see Sections II B 3 and II C 4). In particular, we test values for the c_{max} parameter that range from 300 M to 3 M, which correspond to effective ionic radii from 0.95 Å to 4.39 Å. Introducing a finite size for the ions affects the DC at large applied potentials: while the standard PB model predicts monotonically increasing capacitance values for increasing values of the applied potential, the size-modified model predicts the DC to first reach a maximum and then decrease as the potential deviates from the PZC. The DC maximum is reached at lower values of the potential for decreasing values of the c_{max} parameter. For $c_{max} = 3$ M the DC-potential curve even changes concavity, and the PZC becomes the maximum. The observed DC decrease can be explained by the following arguments. In contrast with the standard PB-model, which allows for infinitely large electrolyte concentrations at the interface boundary, its size-modified variant imposes a maximum local ionic concentration, c_{max} . When this maximum concentration is locally reached, the steric repulsion between the ions pushes the ionic charge density towards the bulk solvent region, effectively increasing the separation between the surface and the electrolyte charge, giving rise to the observed DC decrease.

B. Implicit Solvent

After having investigated the performance of the diffuse layer models in vacuum, we switch to simulations in implicit water and compare results to prototypical experimental data, presented in Figure 9. In particular, we have considered data reported by Valette²¹ on the differential capacitance of Ag(100) in a KPF₆ electrolyte solution. Consistently with commonly-observed experimental trends, the DC exhibits a ‘camel-back’ shape, with the minimum indicating the PZC. As also indicated by Valette, the common potential value at which the potential drop is observed across the various electrolyte concentrations and the rather symmetric shape of the DC curve around the PZC suggest a negligible anion adsorption in this electrolyte solution.

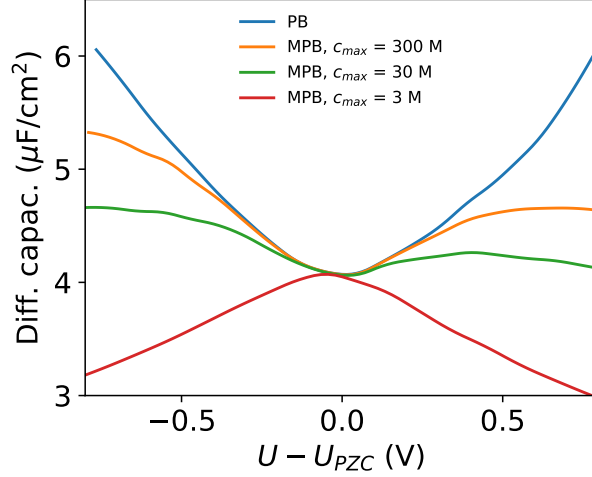


FIG. 8. The differential capacitance is plotted as a function of the potential for various values of the c_{max} parameter in the MPB model. The planar interface function has been used for all calculations, with $d = 6.568$ Bohr and $\Delta = 0.470$ Bohr.

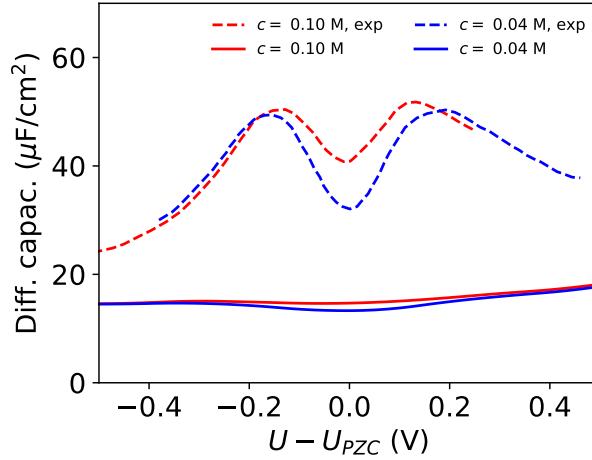


FIG. 9. The differential capacitance is plotted as a function of the potential. Experimental data from Ref.²¹ are plotted as dashed lines. Results of MPB simulations using the SCCS cavity with the original parameterization from Ref.²⁴ are plotted as solid lines. The value of c_{max} is set to 20 M. Red is for $c_0 = 0.1$ M and blue is for $c_0 = 0.04$ M.

On the basis of the results presented in Section III A, only the MPB model is expected to qualitatively reproduce the experimental potential trend, with the capacitance drop at the PZC and the DC saturation and decrease at large applied potentials. Instead, the Helmholtz and the linearized PB model fail to predict the capacitance minimum at the

PZC, and the standard PB model predicts monotonically increasing capacitance curves. Concerning the cavity, the various interface functions have been found to give rise to overall similar capacitance values in vacuum, at least for parameterizations that lead to similar electrolyte charge distributions. The planar and SSCS cavities produce essentially identical results, and for this reason in the following we will consider only the latter, which better suits general interface geometries.

The DC computed with the MPB model and the SSCS interface including the dielectric continuum are plotted in Figure 9. We have used here the original SSCS cavity parameters²⁴, which have been fitted to a database of solvation energies of neutral molecules. We remind, however, that the non-electrostatic solvation terms have been neglected here. Calculations are performed for the experimental bulk electrolyte concentrations (0.1 M and 0.04M) and for the steric repulsion between ions through the c_{max} parameter, which we have initially set to 20 M. Assuming a random close-packing for the ions, this value of c_{max} corresponds to an effective ionic radius of approximately 2.33 Å. In comparison, experimental upper-bounds for the bare (non-solvated) ionic radii are 2.65 Å⁴⁸ and 2.42 Å⁴⁹, for K^+ and PF_6^- , respectively.

As already observed in the vacuum environment, the MPB model predicts a DC drop at the PZC, which is more pronounced for the lowest electrolyte concentration simulated ($c_0 = 0.04$ M). This is in qualitative agreement with measurements. However, the overall absolute magnitude of the DC is severely underestimated, and the potential dependence computed is also much weaker than in experiments.

Figure 10 illustrates how the inclusion of additional solute-electrolyte interactions in the MPB model (see Sections II B 4) affects the computed DC (note the different scale of the y axis). Figure 10A shows the effect of including a solute-electrolyte repulsion potential. This potential introduces a gap between the onset of the dielectric continuum and the one of the electrolyte countercharge density. In particular, we test various values for the distance parameter d in the chosen functional form for the repulsive potential (see Eq. 25). By setting the spread parameter w to 0.25 Å we ensure a fast decay of the exponential repulsion. The effect of introducing this Stern-layer gap is essentially a rigid shift of the DC curve. The observed capacitance decrease is consistent with the corresponding increase of the surface-electrolyte charge distance for increasing d values, and the small magnitude of the shift is related to the large dielectric constant that characterizes the region where the electrolyte

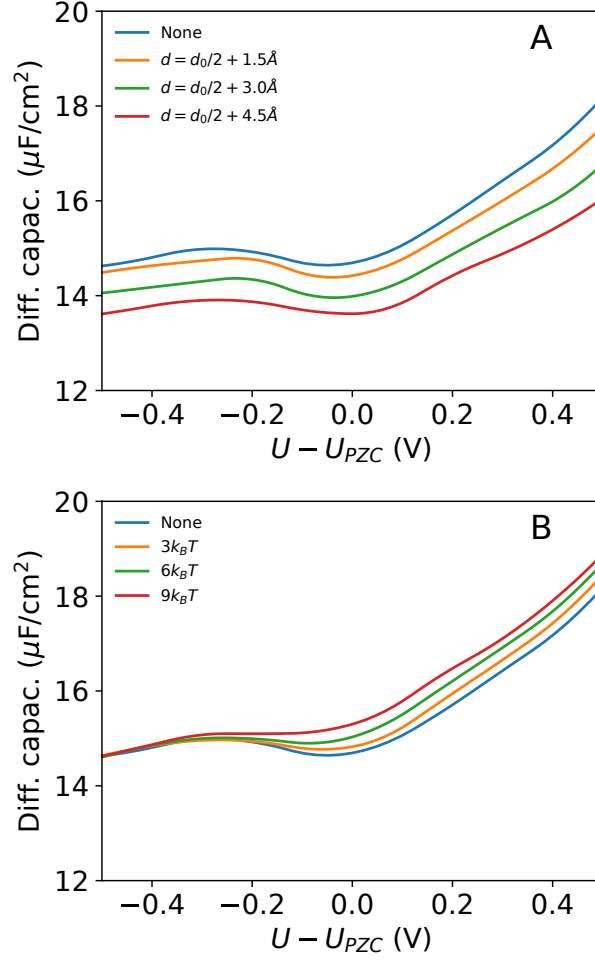


FIG. 10. The differential capacitance plotted as a function of the potential. All data refer to MPB simulations with the SCCS interface. The original parameterization from Ref.²⁴ has been employed, and $c_0 = 0.1$ M and $c_{max} = 20$ M. In the top panel, a repulsive potential between solute and electrolyte is introduced. Different colors correspond to different values of the d parameter, as indicated (w is set to 0.25 \AA). In the bottom panel, a Morse-potential interaction between solute and anions is employed instead, with $d = d_0/2 + 1.5 \text{ \AA}$ and $w = 0.5 \text{ \AA}$. Different colors correspond to different values of the E_{ads} parameter, as indicated.

charge is located.

Figure 10B illustrates how the DC is affected by anion adsorption as accounted through the continuum model of Baskin and Prendergast²⁰. For the solute-anion interactions, we set the following values for the Morse-potential parameters: $w = 0.5 \text{ \AA}$ and $d = d_0/2 + 1.5 \text{ \AA}$, where d_0 is the slab thickness. The adsorption energy E_{ads} is varied in a range from $3k_B T$

to $9k_B T$ (i.e. from 80 meV to 230 meV at 300 K). Note that we simulate the asymmetric anion adsorption without accounting for solute-cation interactions. At the most negative potentials considered, where the electrostatic attraction of cations is much stronger than the imposed solute-anion interaction, the anion adsorption does not alter the computed DC. At the highest potentials simulated, the additional attractive interaction between surface and anions increases the electrolyte countercharge at the interface, thereby increasing the DC. At intermediate potentials, the anion adsorption shifts the DC minimum from the PZC towards negative potentials, where the electrostatic interaction compensates the anion attractive potential.

The cavity parameterization is found to have a much larger influence on the absolute value of the computed DC. This is illustrated in Figure 11, where we plot the DC-potential curves calculated with the original interface parameterization that was optimized for neutral isolated systems and with the two parameterizations that have been later proposed⁵⁰ to best fit anion and cation solvation energies, respectively. The DC computed with the cation-specific parameterization does not significantly differ from the one obtained from the original parameterization. This is consistent with the very similar values for the cavity parameters ρ_{max} and ρ_{min} in the two fits. Significantly different cavity parameters were instead found to best fit the anion database, and we consistently observe a considerable difference in the resulting capacitance. In particular, the anion-specific parameterization is characterized by smaller cavities, and the reduced gap between the surface and the continuum fluids give rise to larger DC values. As illustrated in Figure 10A, the spacing between the surface and the electrolyte countercharge density has a rather contained effect on the absolute DC value. These findings suggest that the gap between the electrode surface and the dielectric polarization charge is thus the main responsible for the large DC dependence on the cavity parameterization, as also suggested by Sundararaman et al.¹⁶. Consistently, Melander *et al.*¹⁷, who have employed a dielectric cavity based on the van der Waals radii of the surface atoms, have found that increasing the atomic radii leads to significantly lower capacitance values.

It is evident that none of the three SCCS cavities described so far is able to describe well experimental data: the original SCCS parameterization and the cation refit underestimate the measured DC, while the anion parameterization overestimates it. This is not surprising, considering that all three parameter sets have been fitted to solvation energies of isolated

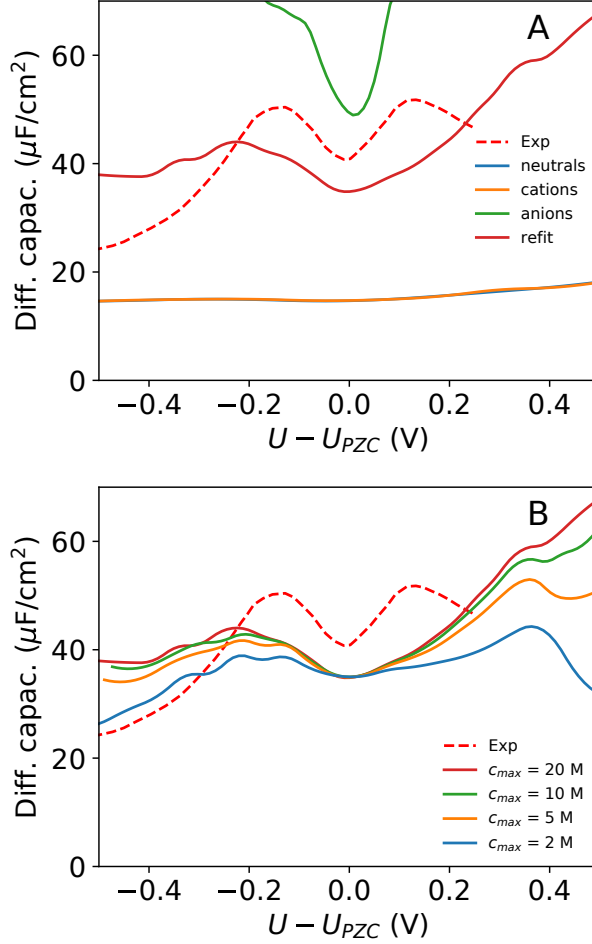


FIG. 11. The differential capacitance is plotted as a function of the potential for $c_0 = 0.1$ M. Experimental data²¹ are shown as dashed lines. All theoretical data refer to MPB simulations with the SCCS interface function. In the top panel, results from the original SCCS parameterization²⁴ ('neutral'), are compared to results from the cation- and anion-specific parameterizations⁵⁰ and to results from the parameter fit to the Pt(111) PZC⁵¹. The value of c_{max} is set to 20 M. In the bottom panel, the SCCS parameterization from Ref.⁵¹ is employed, and the value of c_{max} varied from 20 M to 2 M, as indicated.

systems. Figure 11A also includes a DC curve computed with cavity parameters that have been recently fitted⁵¹ to reproduce the theoretical estimate of the absolute PZC of Pt(111). This last parameterization overall returns the best agreement with experimental data, even though it underestimates the measured DC in the potential region close to the PZC and more severely overestimates it for larger applied potentials.

As clearly shown from the simulations in vacuum, the capacitance of the MPB model at large absolute potentials is strongly affected by the steric-repulsion between the ions (cf. Figure 8). Figure 11B shows the effect of decreasing the value of c_{max} from 20 M to 2 M, which is equivalent to increasing the ionic particle radii from 2.33 Å to 5.02 Å. Decreasing c_{max} broadens the minimum in correspondence of the PZC and lower the capacitance at the highest and lowest potentials examined, improving agreement with experimental data. It is thus tempting to suggest that effective radii larger than the bare ones should be employed for the electrolyte particles, as also suggested in the literature on the basis of the strongly-bound solvent molecules surrounding ions in solution¹⁸. Note that experimental estimates for the radius of the solvated K^+ ions span a range¹⁸ from 3.8 Å⁵² to 6.62 Å⁵³, which would largely justify the range of c_{max} investigated.

After having investigated the DC capacitance computed using density-based cavities, we now consider simulations performed with the SSCS interface function. Results are presented in Figure 12, where we have used the parameterization proposed by Fisicaro et al.²⁸. Figure 12A reports the capacitance computed using the upper-bound c_{max} value of 20 M. Despite the cavity parameters were originally fitted to solvation energies of isolated systems as for the SSCS interface, the SSCS model leads to a very good description of the experimental DC around the PZC for the two electrolyte concentrations considered. As also observed for the SSCS interface function, the capacitance at large absolute potentials is instead overestimated when using $c_{max} = 20$ M. Similar to the case of vacuum (Section III A), the (M)PB model returns asymmetric DC curves with the rigid cavity from the SSCS model. This finding can again be explained on the basis of the extent by which the electron density spilling from the metal surface approaches the continuum. The separation between the surface and the electrolyte onset, in fact, is effectively reduced for lower values of the potential, with a subsequent increase of the capacitance values.

Figure 12B shows the computed DC curve for the lower c_{max} value of 2 M ($r_i = 5.02$ Å). The agreement with experiments is significantly improved, and both the position and the height of the ‘humps’ are comparable to measured data. Thus, also calculations performed with the SSCS cavity suggest that ionic radii larger than the bare ones should be employed to limit the steric crowding at electrode interfaces. Note that Sundararaman et al. recently achieved a similarly good description of the DC of Ag(100) with a soft-sphere-based continuum model¹⁶. The cavity size in their model was also based on the Ag ionic radius

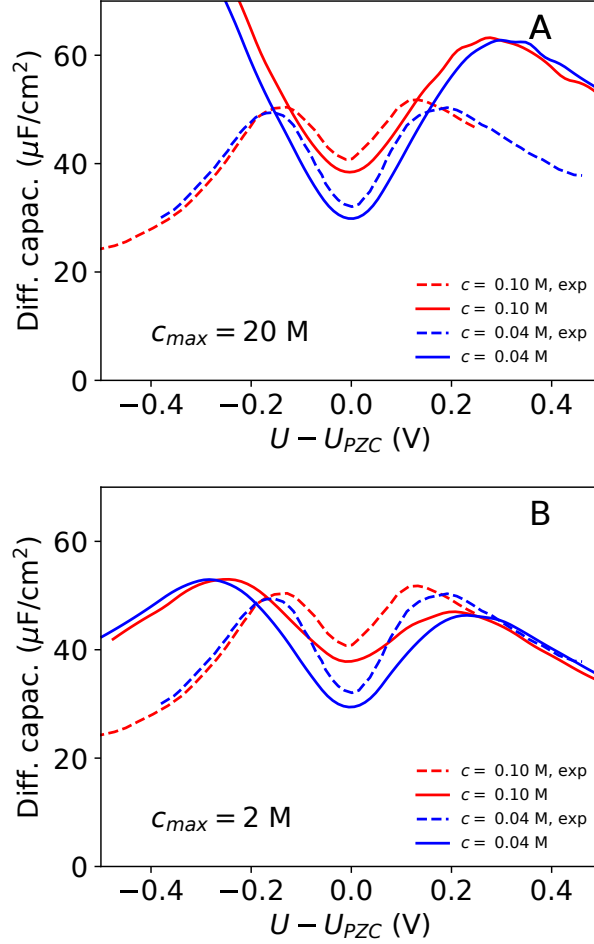


FIG. 12. Same as Figure 9, but the SSCS interface has been employed in the simulations. In top and bottom panel the value of c_{max} is set to 20 M and 2 M, respectively.

as tabulated in the unified force-field (UFF)⁵⁴, times a scaling constant. As also noted by Sundararaman et al.¹⁶, the good description of the Ag(100) DC might be thus inferred to the Ag UFF ionic radius being fortuitously suitable to describe the cavity size for this system. Future investigations of the DC for other systems will shed light on this point.

Despite the overall good agreement with experimental data, the DC predicted using the SSCS cavity overestimates and underestimates the measured data at negative and positive potentials, respectively. The trend observed with the soft-sphere cavity in implicit solvent is consistent with the trends observed in vacuum with rigid cavities, which are found to predict an overall decreasing DC with increasing potential. In comparison, measurements exhibit slightly larger capacitance values at positive potentials, in better agreement with trends observed with the density-dependent SSCS cavity. Future work will clarify whether

improved agreement with experimental data can be achieved by a specific refitting of the SCCS cavity.

Regardless on the cavity employed, our findings suggest that the MPB model for the electrolyte is able to capture the main features of the experimental DC for Ag(100) in an ideally non-adsorbing ionic solution. We note in passing that in addition of being more physically sound, the MPB model is also more numerically stable than the standard PB model, as the extremely large ionic charge densities that the latter predicts at the boundary between the electrified surface and the solvent region are difficult to handle with the numerical solvers without the inclusion of a Stern layer. While avoiding such instabilities, the linearized-PB model is inadequate for describing the capacitance of a charged metal surface. As expected from the results in vacuum (Section III A), Figure 13 illustrates how the linear-regime model predicts essentially potential-independent capacitance values, which are only accurate close to the PZC.

Our results are in contrast with the finding from Ref.¹⁶, where an additional non-linear dielectric model was suggested to be necessary in order to reproduce the trends observed in the measurements. Our findings also differ from the ones of Melander *et al.*¹⁷, who have reported potential-independent capacitance trends for a metal surface (Au(210)) in an electrolyte solution using both a linearized- and a non-linear- MPB model. While discrepancies with Refs.^{16,17} require further investigation, our results are consistent with data from full-continuum models^{18–20}, where the solution of the non-linear MPBE is found to lead to the experimentally-observed ‘camel-back’-shape for the DC curve for metal surfaces in aqueous solutions.

IV. SUMMARY AND CONCLUSIONS

In summary, we have presented a hierarchy of electrolyte models that can be integrated in the framework of DFT to account for the presence of the diffuse layer in first-principles simulations of electrochemical interfaces. We have validated the accuracy of the models by comparing computed DC values to experimental data, focusing on the Ag(100) surface in an aqueous electrolyte as study system.

Results suggest that the size-modified PB model is necessary in order to reproduce the main characteristics of the experimental DC, i.e. the concentration-dependent drop at the

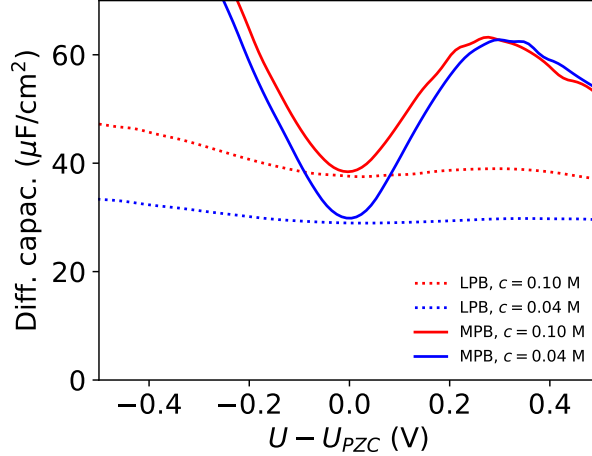


FIG. 13. Same as Figure 12, but the DC curves obtained with the MPB model and $c_{max} = 20$ M are compared to analogous curves obtained with the linearized PB model.

PZC and the two local maxima at intermediate applied potentials. The lowest-rung planar Helmholtz model, which does not include any dependence on the bulk electrolyte concentration, predicts negligible DC dependences on the applied potential. Similarly, the standard PB model, both in the linear-regime and in its full non-linear implementations fails in describing experimental DC trends.

Further accounting for solvent effects through a continuum dielectric allows for a direct comparison of computed DC values to experimental data. We observe a large influence of the choice of the dielectric cavity on the absolute DC values, consistently with previous findings^{15,16}. For the SCCS interface function, the best agreement with experimental data is obtained for a parameterization of the cavity that is fitted⁵¹ to reproduce an interface-related observable, i.e. the theoretical estimate of the PZC of Pt(111). The original parameterization of the SSCS cavity has been found instead to produce a relatively good agreement with experimental data without the need of refitting.

While it is important to stress how the different approaches can be extended and tuned to improve the description of electrochemical systems, it is worth pointing out that the reported analysis is based on continuum models that only account for part of the physical phenomena occurring at electrified interfaces. At the center of the reported analysis is the description of the diffuse layer, of its shape and characteristics. Nonetheless, a more realistic model should account for the different sizes of the ions composing the electrolyte. Moreover, as it is also

clear from the results reported, the dielectric properties of the liquid solution at the interface with a solid substrate need to be properly modeled in order for the continuum approach to be meaningful. The bare substrate and, even more, a charged interface will induce order and rigidity in the overlaying liquid, substantially affecting the dielectric permittivity over a distance of one or more solvation layers. The fact that current state-of-the-art continuum models are not able to describe with the same accuracy systems with different charge states, and in particular require a separate parameterization for anions, is clearly a limitation of the current techniques in dealing with electrified interfaces. Similarly, non-linear effects in the dielectric response of the liquid may account for some of the deviations observed at higher applied potentials. Other possibly minor effects that are not explicitly accounted for in the presented models are the ones related to the change in dielectric screening of the electrolyte solution for high concentrations of the diffuse layer. Cancellation of errors resulting from the parameterization of the model may lead to an approach that seems accurate, but lacks transferability. As more and more ingredients are added and carefully tuned, they will unlock the full potential of continuum models for electrochemical setups.

ACKNOWLEDGMENTS

This project has received funding from the European Union’s Horizon 2020 research and innovation programme under grant agreements No. 665667 and No. 798532. N. M. and O. A. acknowledge partial support from the MARVEL National Centre of Competence in Research of the Swiss National Science Foundation. This work was supported by a grant from the Swiss National Supercomputing Centre (CSCS) under project ID s836. Part of the computational developments presented in this work have been pursued during the UNT Hackathon 2018, sponsored by the ORAU Envent Sponsorship Program and the University of North Texas.

REFERENCES

- ¹P. Simon and Y. Gogotsi, [Nat. Mater.](#) **7**, 845 (2008).
- ²P. M. Biesheuvel, A. A. Franco, and M. Z. Bazant, [J. Electrochem. Soc.](#) **156**, B225 (2009).

- ³K.-Y. Yeh and M. J. Janik, in *Computational Catalysis*, edited by A. Asthagiri and M. J. Janik (Royal Society of Chemistry, 2013) pp. 116–156.
- ⁴C. L. Fu and K. M. Ho, *Phys. Rev. Lett.* **63**, 1617 (1989).
- ⁵A. Y. Lozovoi and A. Alavi, *Phys. Rev. B* **68**, 245416 (2003).
- ⁶N. Bonnet and N. Marzari, *Phys. Rev. Lett.* **110**, 086104 (2013).
- ⁷M. Otani and O. Sugino, *Phys. Rev. B* **73**, 115407 (2006).
- ⁸R. Jinnouchi and A. B. Anderson, *Phys. Rev. B* **77**, 245417 (2008).
- ⁹I. Dabo, *Towards first-principles electrochemistry*, *Ph.D. thesis*, Massachusetts Institute of Technology (2008).
- ¹⁰I. Dabo, E. Cancès, Y. L. Li, and N. Marzari, *arXiv* , 0901.0096 (2008).
- ¹¹I. Dabo, Y. Li, N. Bonnet, and N. Marzari, in *Fuel Cell Science*, edited by A. Wiecowski and J. Nørskov (John Wiley & Sons, 2010) pp. 415–431.
- ¹²K. Letchworth-Weaver and T. A. Arias, *Phys. Rev. B* **86**, 75140 (2012).
- ¹³D. Gunceler, K. Letchworth-Weaver, R. Sundararaman, K. A. Schwarz, and T. A. Arias, *Model. Simul. Mater. Sci. Eng.* **21**, 074005 (2013).
- ¹⁴K. Mathew and R. G. Hennig, *arXiv* , 1601.03346 (2016).
- ¹⁵R. Sundararaman and K. Schwarz, *J. Chem. Phys.* **146**, 084111 (2017).
- ¹⁶R. Sundararaman, K. Letchworth-Weaver, and K. A. Schwarz, *J. Chem. Phys.* **148**, 144105 (2018).
- ¹⁷M. Melander, M. Kuisma, T. Christensen, and K. Honkala, *ChemRxiv* (2018).
- ¹⁸M. Z. Bazant, M. S. Kilic, B. D. Storey, and A. Ajdari, *Adv. Colloid Interface Sci.* **152**, 48 (2009).
- ¹⁹Y. Nakayama and D. Andelman, *J. Chem. Phys.* **142**, 044706 (2015).
- ²⁰A. Baskin and D. Prendergast, *J. Electrochem. Soc.* **164**, E3438 (2017).
- ²¹G. Valette, *J. Electroanal. Chem. Interfacial Electrochem.* **138**, 37 (1982).
- ²²J.-L. Fattebert and F. Gygi, *Int. J. Quantum Chem.* **93**, 139 (2003).
- ²³D. A. Scherlis, J. L. Fattebert, F. Gygi, M. Cococcioni, and N. Marzari, *J. Chem. Phys.* **124**, 74103 (2006).
- ²⁴O. Andreussi, I. Dabo, and N. Marzari, *J. Chem. Phys.* **136**, 64102 (2012).
- ²⁵O. Stern, *Z. Elektrochem.* **30**, 508 (1924).
- ²⁶R. C. Harris, A. H. Boschitsch, and M. O. Fenley, *J. Chem. Phys.* **140**, 075102 (2014).
- ²⁷S. Ringe, H. Oberhofer, C. Hille, S. Matera, and K. Reuter, *J. Chem. Theory Comput.*

- [12](#), 4052 (2016).
- ²⁸G. Fiscaro, L. Genovese, O. Andreussi, S. Mandal, N. N. Nair, N. Marzari, and S. Goedecker, [J. Chem. Theory Comput.](#) **13**, 3829 (2017).
- ²⁹M. Cococcioni, F. Mauri, G. Ceder, and N. Marzari, [Phys. Rev. Lett.](#) **94**, 145501 (2005).
- ³⁰H. Helmholtz, [Ann. Phys.](#) **165**, 211 (1853).
- ³¹I. Borukhov, D. Andelman, and H. Orland, [Phys. Rev. Lett.](#) **79**, 435 (1997).
- ³²M. Gouy, [J. Phys. Theor. Appl.](#) **9**, 457 (1910).
- ³³D. L. Chapman, [Philos. Mag.](#) **25**, 475 (1913).
- ³⁴I. Borukhov, D. Andelman, and H. Orland, [Electrochim. Acta](#) **46**, 221 (2000).
- ³⁵S. Ringe, H. Oberhofer, and K. Reuter, [J. Chem. Phys.](#) **146**, 134103 (2017).
- ³⁶O. Andreussi and N. Marzari, [Phys. Rev. B](#) **90**, 245101 (2014).
- ³⁷G. Fiscaro, L. Genovese, O. Andreussi, N. Marzari, and S. Goedecker, [J. Chem. Phys.](#) **144**, 014103 (2016).
- ³⁸O. Andreussi, F. Nattino, I. Dabo, I. Timrov, G. Fiscaro, G. S., and N. Marzari, [www.quantum-environment.org](#) (2018).
- ³⁹P. Giannozzi, S. Baroni, N. Bonini, M. Calandra, R. Car, C. Cavazzoni, D. Ceresoli, G. L. Chiarotti, M. Cococcioni, I. Dabo, A. D. Corso, S. D. Gironcoli, S. Fabris, G. Fratesi, R. Gebauer, U. Gerstmann, C. Gougoussis, A. Kokalj, M. Lazzeri, L. Martin-samos, N. Marzari, F. Mauri, R. Mazzarello, S. Paolini, A. Pasquarello, L. Paulatto, C. Sbraccia, A. Smogunov, and P. Umari, [J. Phys.: Condens. Matter](#) **21**, 395502 (2009).
- ⁴⁰P. Giannozzi, O. Andreussi, T. Brumme, O. Bunau, M. Buongiorno Nardelli, M. Calandra, R. Car, C. Cavazzoni, D. Ceresoli, M. Cococcioni, N. Colonna, I. Carnimeo, A. Dal Corso, S. de Gironcoli, P. Delugas, R. A. DiStasio, A. Ferretti, A. Floris, G. Fratesi, G. Fugallo, R. Gebauer, U. Gerstmann, F. Giustino, T. Gorni, J. Jia, M. Kawamura, H.-Y. Ko, A. Kokalj, E. Küçükbenli, M. Lazzeri, M. Marsili, N. Marzari, F. Mauri, N. L. Nguyen, H.-V. Nguyen, A. Otero-de-la Roza, L. Paulatto, S. Poncé, D. Rocca, R. Sabatini, B. Santra, M. Schlipf, A. P. Seitsonen, A. Smogunov, I. Timrov, T. Thonhauser, P. Umari, N. Vast, X. Wu, and S. Baroni, [J. Phys.: Condens. Matter](#) **29**, 465901 (2017).
- ⁴¹J. P. Perdew, K. Burke, and M. Ernzerhof, [Phys. Rev. Lett.](#) **77**, 38653868 (1996).
- ⁴²J. P. Perdew, K. Burke, and M. Ernzerhof, [Phys. Rev. Lett.](#) **78**, 1396 (1997).
- ⁴³K. F. Garrity, J. W. Bennett, K. M. Rabe, and D. Vanderbilt, [Comput. Mat. Sci.](#) **81**, 446 (2014).

- ⁴⁴G. Prandini, A. Marrazzo, I. E. Castelli, N. Mounet, and N. Marzari, [arXiv , 1806.05609 \(2018\)](#).
- ⁴⁵N. Marzari, D. Vanderbilt, A. De Vita, and M. C. Payne, [Phys. Rev. Lett. **82**, 3296 \(1999\)](#).
- ⁴⁶O. Andreussi, N. Hörmann, F. Nattino, and N. Marzari, In preparation (2018).
- ⁴⁷M. N. Tamashiro and H. Schiessel, [Phys. Rev. E **68**, 066106 \(2003\)](#).
- ⁴⁸R. Mancinelli, A. Botti, F. Bruni, M. A. Ricci, and A. K. Soper, [J. Phys. Chem. B **111**, 13570 \(2007\)](#).
- ⁴⁹H. K. Roobottom, H. D. B. Jenkins, J. Passmore, and L. Glasser, [J. Chem. Educ. **76**, 1570 \(1999\)](#).
- ⁵⁰C. Dupont, O. Andreussi, and N. Marzari, [J. Chem. Phys. **139**, 214110 \(2013\)](#).
- ⁵¹N. Hörmann, O. Andreussi, and N. Marzari, Submitted to J. Chem. Phys. (2018).
- ⁵²K. L. Gering, [Electrochim. Acta **51**, 3125 \(2006\)](#).
- ⁵³E. R. Nightingale, [J. Phys. Chem. **63**, 1381 \(1959\)](#).
- ⁵⁴A. K. Rappe, C. J. Casewit, K. S. Colwell, W. A. Goddard, and W. M. Skiff, [J. Am. Chem. Soc. **114**, 10024 \(1992\)](#).